*catalysts*

MDPI

*Article*

# Effect of Fe and Mn Substitution in $LaNiO_3$ on Exsolution, Activity, and Stability for Methane Dry Reforming

**Eswaravara Prasadarao Komarala** †, **Ilia Komissarov** † and **Brian A. Rosen** *

Department of Materials Science and Engineering, Tel Aviv University, Ramat Aviv 6997801, Israel; einwar2020@gmail.com (E.P.K.); iliakom1000@gmail.com (I.K.)
* Correspondence: barosen@post.tau.ac.il
† Authors with equal contribution.

Received: 1 December 2019; Accepted: 21 December 2019; Published: 25 December 2019

**Abstract:** Perovskites $LaNi_{0.8}Fe_{0.2}O_3$ and $LaNi_{0.8}Mn_{0.2}O_3$ were synthesized using the co-precipitation method by substituting 20 mol.% of the Ni-site with Fe and Mn, respectively. Temperature programmed reduction (TPR) showed that the exsolution process in the Fe- and Mn-substituted perovskites followed a two-step and three-step reduction pathway, respectively. Once exsolved, the catalysts were found to be able to regenerate the original perovskite when exposed to an oxygen environment but with different crystallographic properties. The catalytic activity for both materials after exsolution was measured for the methane dry reforming (DRM) reaction at 650 °C and 800 °C. Catalyst resistance against nickel agglomeration, unwanted phase changes, and carbon accumulation during DRM were analyzed using X-ray diffraction (XRD), transmission electron microscopy (TEM), and thermogravimetric analysis (TGA). The presence Fe alloying in the catalyst particles after exsolution from $LaNi_{0.8}F_{e0.2}O_3$ led to a lower methane conversion compared to the catalyst derived from $LaNi_{0.8}Mn_{0.2}O_3$ where no alloying occurred.

**Keywords:** smart catalysts; regenerating catalysts; perovskites; solid-phase crystallization

## 1. Introduction

Recently, the dry reforming of methane (DRM, Reaction 1) has gained considerable attention due to its ability to produce synthesis gas via the simultaneous consumption of two greenhouse gases, methane ($CH_4$), and carbon dioxide ($CO_2$) [1,2]. Synthesis gas generated by this process can then be converted to synthetic liquid hydrocarbon fuels through the industrially well-known Fischer–Tropsch reaction [3]:

$$CH_4 + CO_2 \rightleftharpoons 2CO + 2H_2, \quad \Delta H^o_{298K} = 247.3 \text{ kJ/mol}. \tag{1}$$

The DRM reaction is typically accompanied by side-reactions which serve both to decrease the $H_2$:CO ratio (reverse water–gas shift reaction, RWGS) as well as lead to solid carbon accumulation (e.g., deep methane cracking, Boudouard reaction, etc.) as shown in Equations (2)–(4):

$$CO_2 + H_2 \rightleftharpoons CO + H_2O, \quad \Delta H^o_{298K} = 41.2 \text{ kJ/mol}, \tag{2}$$

$$CH_4 \rightleftharpoons C(s) + 2H_2, \quad \Delta H^o_{298K} = 74.9 \text{ kJ/mol}, \tag{3}$$

$$2CO \rightleftharpoons C(s) + CO_2, \quad \Delta H^o_{298K} = -173.5 \text{ kJ/mol}. \tag{4}$$

Interestingly, solid carbon formation on the catalyst surface is both a necessary mechanistic step for methane conversion and also a source for catalyst deactivation via coking [4]. Surface carbon is broken down into five different categories including: atomic, amorphous, vermicular, graphitic, and metal carbides. Atomic carbon is easily gasified by incoming oxidizing agents, whereas whiskers, fibers, and graphitic accumulation limit the application of methane dry reforming because they cause rapid catalyst deactivation [5].

The DRM has been previously investigated on many catalysts based on noble and transition metal elements. Although noble-metal catalysts are active and less sensitive to carbon accumulation, Ni-based catalysts are preferred due to their ability to activate the C–H bond, relatively low cost, and availability [6–9]. It is well known though that Ni-based catalysts suffer from deactivation during DRM largely owing to coking and sintering [10,11].

Many efforts have been made to synthesize highly-active yet resistant Ni-based catalyst; however, the potential drawback to some of these methods is the superficial interaction between the Ni metal and the catalyst support, exacerbating both the coking and sintering mechanisms [12,13]. Solid-phase crystallization (also known as exsolution) is an alternative method to incipient wetness impregnation for the preparation of supported catalysts where reducible metal ions are exsolved from the lattice, typically from perovskites ($ABO_3$) [14]. This method produces a supported catalyst by dispersing metal nanoparticles on the residual oxide through selective cation reduction in a heated reducing atmosphere. The solid-phase crystallization technique has been used to synthesize various catalysts using $LaCoO_3$, $LaFeO_3$, $LaMnO_3$, and $LaNiO_3$ as precursors [15–20]. The focus of most studies has been the properties of the exsolved nanoparticle, and comparatively less to the released oxide(s), which ultimately serve as the support.

Various strategies have been suggested to improve the coke resistance of exsolved catalysts derived from perovskites. Partial A-site substitution with rare-earth elements have been used to improve the oxygen mobility and adsorption of $CO_2$ [21,22]. Partial B-site substitution by transition metals has been used for regulating methane adsorption and activation [23]. Substituting Ni with transition metals like Co, Fe, and Mn has also been investigated for activity and stability towards DRM reaction, but results have varied [24–29].

Furthermore, the regenerative property of some exsolved catalysts can repair damage caused by agglomeration by regenerating the perovskite in an oxygen environment, additionally gasifying carbon deposits. The perovskite may then be reactivated in a reducing environment to regenerate the supported catalyst. The regenerative property of Ni-based perovskites has been scarcely studied as compared to Pd (e.g., $LaFe_{1-x}Pd_xO_3$) [30–32].

In this work, the effect of B-site substation into the $LaNiO_3$ perovskite by Fe and Mn is studied with respect to the ability for the Ni particles to be re-dispersed through regeneration, as well as activity, stability, and selectivity for methane dry reforming. Such factors are of high importance for the development of industrial dry reforming catalysts using the exsolution method.

## 2. Results and Discussion

### *2.1. Catalyst Formation and Regeneration*

The structure and morphology of as-synthesized perovskites were characterized by X-ray diffraction (XRD) and SEM and given in Figure 1. The XRD patterns in Figure 1a show that both the samples are crystalline perovskites with a rhombohedral structure and close to the parent $LaNiO_3$ (PDF 04-006-7137). The XRD pattern of $LaNi_{0.8}Mn_{0.2}O_3$ showed a slight shift towards a lower angle side as compared to that of $LaNi_{0.8}Fe_{0.2}O_3$ (as shown in Figure 1b) due to the fact that the size of $Mn^{+3}$ is larger than that of $Fe^{+3}$ [33,34].

SEM images in Figure 1c,d show that both $LaNi_{0.8}Fe_{0.2}O_3$ and $LaNi_{0.8}Mn_{0.2}O_3$ perovskites had a spheroid morphology. Energy dispersive X-ray spectroscopic (EDS) elemental mapping of both perovskites (Figures S1 and S2) show the uniform distribution of elements over the sample and the presence of both Fe and Mn in $LaNi_{0.8}Fe_{0.2}O_3$ and $LaNi_{0.8}Mn_{0.2}O_3$ perovskites, respectively. From both XRD and SEM analysis, it is clear that the partial substitution of Fe or Mn at B-site of $LaNiO_3$ did not disturb the parent perovskite structure or particle morphology.

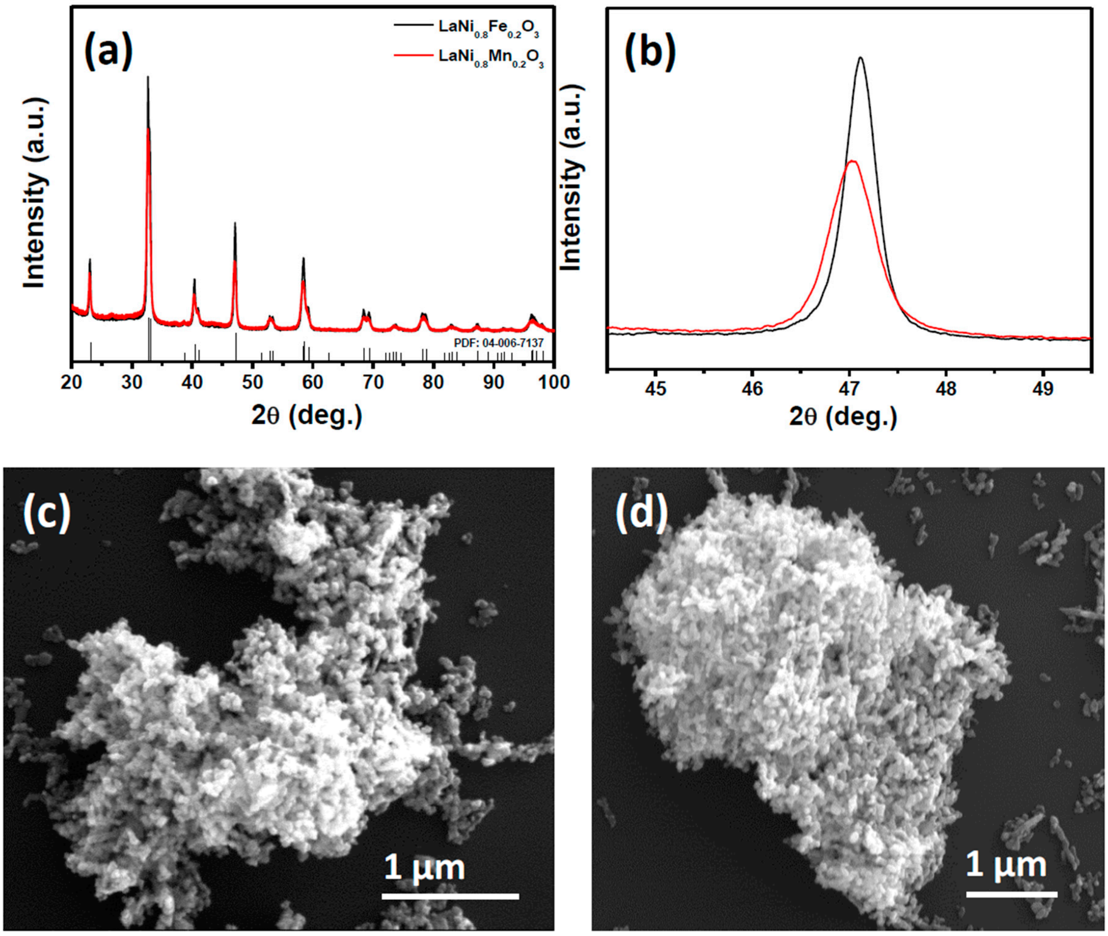

**Figure 1.** (**a**) XRD pattern of as-synthesized $LaNi_{0.8}Fe_{0.2}O_3$ and $LaNi_{0.8}Mn_{0.2}O_3$ perovskites; (**b**) (200) reflection; SEM images of as-synthesized; (**c**) $LaNi_{0.8}Fe_{0.2}O_3$; and (**d**) $LaNi_{0.8}Mn_{0.2}O_3$ perovskites.

Temperature programmed reduction (TPR) of both $LaNi_{0.8}Fe_{0.2}O_3$ and $LaNi_{0.8}Mn_{0.2}O_3$ perovskites was used in order to compare the exsolution of Ni and the formation of sub-oxides in the support. Figure 2 shows that both materials exhibited distinct low-temperature reduction peaks (<650 °C) and high-temperature reduction peaks (>650 °C). The parent $LaNiO_3$ perovskite is known to exsolve Ni using either a 2-step or a 3-step pathway, depending on the defect structure [35,36]. Based on these pathways, the first peak in the $LaNi_{0.8}Mn_{0.2}O_3$ reduction could be due to the formation of the $La_4Mn_xNi_{3-x}O_{10}$ Ruddlesden–Popper (RP) phase, where Mn remains substituted in Ni lattice positions. The second reduction peak could therefore be due to the formation of the $La_2Ni_xMn_{1-x}O_4$ RP phase. Reduction peaks above 600 °C are associated with the formation of $MnO_{1-\delta}$, $Mn_3O_4$, and $La_2O_3$. The reduction of $LaNi_{0.8}Fe_{0.2}O_3$ appeared to coincide with the 2-step reduction pathway through the formation of a Brownmillerite intermediate phase, $La_2Fe_xNi_{2-x}O_5$. Additional peaks above 600 °C are attributed to the final reduction forming alloyed Ni-Fe nanoparticles as well as the partial reduction of $Fe^{3+}$ to $Fe^{2+}$ [37,38].

Interestingly, this temperature of each major reduction step in the substituted perovskites is slightly higher compared to the analogous reduction steps in un-substituted $LaNiO_3$ [36]. This suggests that substitution with both Fe and Mn increases the average cation-oxygen bond strength and therefore the stability of the parent perovskite.

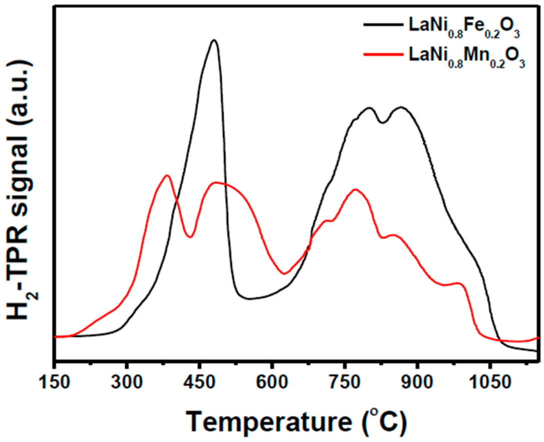

**Figure 2.** Temperature programmed reduction of $LaNi_{0.8}Fe_{0.2}O_3$ and $LaNi_{0.8}Mn_{0.2}O_3$ perovskites performed under 5% $H_2$ atmosphere.

Ni was exsolved from the Fe- and Mn-substituted structures using 5 vol.% $H_2$/Ar at 800 °C for 2 h. Exsolved catalysts were recovered to their perovskite precursors using 50 vol.% $O_2$/Ar atmosphere at 800 °C for 8 h. The long oxidation time (compared to the 2 h reduction) results from the fact that the oxidation process and solid-state diffusion comparatively slow [39]. Catalysts which suffer from agglomeration to larger particles therefore require longer times to recover. Figure 3 shows in-situ XRD of exsolution, regeneration, and re-exsolution for both Fe- and Mn-substituted perovskites.

The exsolution of Ni phases (Ni-Fe alloy for $LaNi_{0.8}Fe_{0.2}O_3$ and pure Ni for $LaNi_{0.8}Mn_{0.2}O_3$) after reduction of both perovskites is apparent from both XRD (Figure 3a,b) and TEM images (Figure 3e,f). After the regeneration step in oxygen, XRD shows the recovery of the original perovskite phase, matching well with the patterns of the as-synthesized samples. TEM images (Figure 3g,h) show that the Ni phases exsolved from the exsolution step have been removed and reincorporated into the support oxide to regenerate the perovskite.

Once recovered, a second exsolution was performed to form Ni nanoparticles from the recovered perovskite, and is shown in Figure 3i,j. The XRD patterns from the two different exsolution steps match well with each other. Interestingly, the $La(OH)_3$ phase, which was formed after the first exsolution of Ni from $LaNi_{0.8}Mn_{0.2}O_3$, was not present after the second exsolution, likely due to the evacuation of residual moisture during the recovery step.

X-ray diffraction (XRD) and Reitveld fitting using TOPAS was used in order to evaluate how the domain size for the supporting perovskite phase and the exsolved crystals changed between the as-synthesized and recovered material. Table 1 shows that both $LaNi_{0.8}Fe_{0.2}O_3$ and $LaNi_{0.8}Mn_{0.2}O_3$ had similar domain sizes as-synthesized. Upon exsolution, the Ni-Fe nanoparticles exsolved from $LaNi_{0.8}Fe_{0.2}O_3$ were 11 nm, less than half the size of Ni exsolved from $LaNi_{0.8}Mn_{0.2}O_3$ (28 nm). Upon recovery in oxygen, the domain size for both perovskites was significantly smaller than their original values. This may be expected since the first exsolution caused significant phase changes and therefore rearranged the grain structure. After a second exsolution cycle, both materials grew catalytic nanoparticles of approximately the same size.

**Table 1.** XRD Domain Size from Reitveld Analysis (nm).

| | $LaNi_{0.8}Fe_{0.2}O_3$ | $LaNi_{0.8}Mn_{0.2}O_3$ | Ni-Fe from $LaNi_{0.8}Fe_{0.2}O_3$ | Ni from $LaNi_{0.8}Mn_{0.2}O_3$ |
|---|---|---|---|---|
| **As synthesized** | 334 | 377 | | |
| **Exsolution #1** | | | 11 | **28** |
| **Recovered** | 51 | 22 | | |
| **Exsolution #2** | | | 11 | **10** |

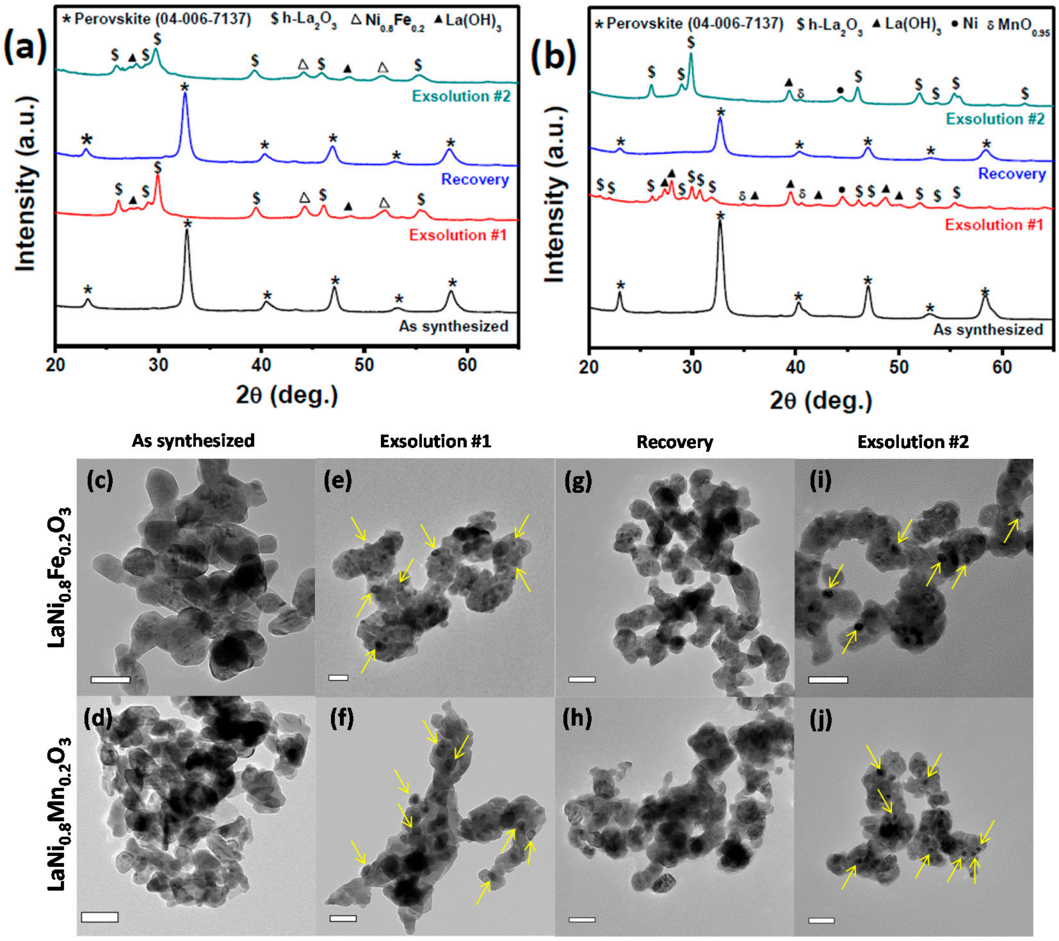

**Figure 3.** XRD patterns after exsolved and recovered catalysts (**a**) $LaNi_{0.8}Fe_{0.2}O_3$ perovskite; (**b**) $LaNi_{0.8}Mn_{0.2}O_3$ perovskite; TEM images of as synthesized; (**c**) $LaNi_{0.8}Fe_{0.2}O_3$; and (**d**) $LaNi_{0.8}Mn_{0.2}O_3$ perovskites (**e**,**f**) after first exsolution, (**g**,**h**) after recovery in oxygen for 8 h at 800 °C (**i**,**j**) second exsolution after recovery. Few exsolved NiFe/Ni nanoparticles in both perovskites after each exsolution step are marked by yellow arrows. Scale bars in all TEM images are 50 nm.

Interestingly, the size of Ni-Fe remained unchanged (11 nm) between the first and second exsolution cycle, whereas the Ni nanoparticles decreased to half the size upon exsolving from the recovered perovskite.

### 2.2. Catalytic Activity for Dry Reforming of Methane (DRM)

Catalysts exsolved from $LaNi_{0.8}Fe_{0.2}O_3$ and $LaNi_{0.8}Mn_{0.2}O_3$ perovskites were tested in order to compare the effect of the 20% B-site substitution with either Fe or Mn on activity and stability under methane dry reforming conditions at 650 °C and at 800 °C. This allowed for comparison under conditions where the Boudouard reaction is favored (Reaction 4), where deep methane cracking is favored (Reaction 3) [40], as well as the effect of temperature on agglomeration. To evaluate catalytic activity and stability, a 1:1 molar ratio of $CH_4$ and $CO_2$ were fed to the catalyst at a gas-hourly space velocity (GHSV) of 13,700 mL/($g_{cat}$·h). Figure 4a,b show that the $CO_2$ conversion of the catalysts at both temperatures is slightly higher than $CH_4$ conversion. This can be attributed to the occurrence of reverse water gas shift reaction (RWGS, Equation (2)), which also consumes $CO_2$ along with the DRM reaction resulting in a $H_2$:CO product ratio less than unity [41,42]. At both temperatures, the catalyst derived from reduced $LaNi_{0.8}Mn_{0.2}O_3$ catalyst showed higher conversion than that derived from reduced $LaNi_{0.8}Fe_{0.2}O_3$ (Figure 4a,b). The reduced $LaNi_{0.8}Fe_{0.2}O_3$ catalyst showed stable conversion after a small initial decrease in conversion. This is explained by the de-alloying of the exsolved Ni-Fe particle, to be discussed below.

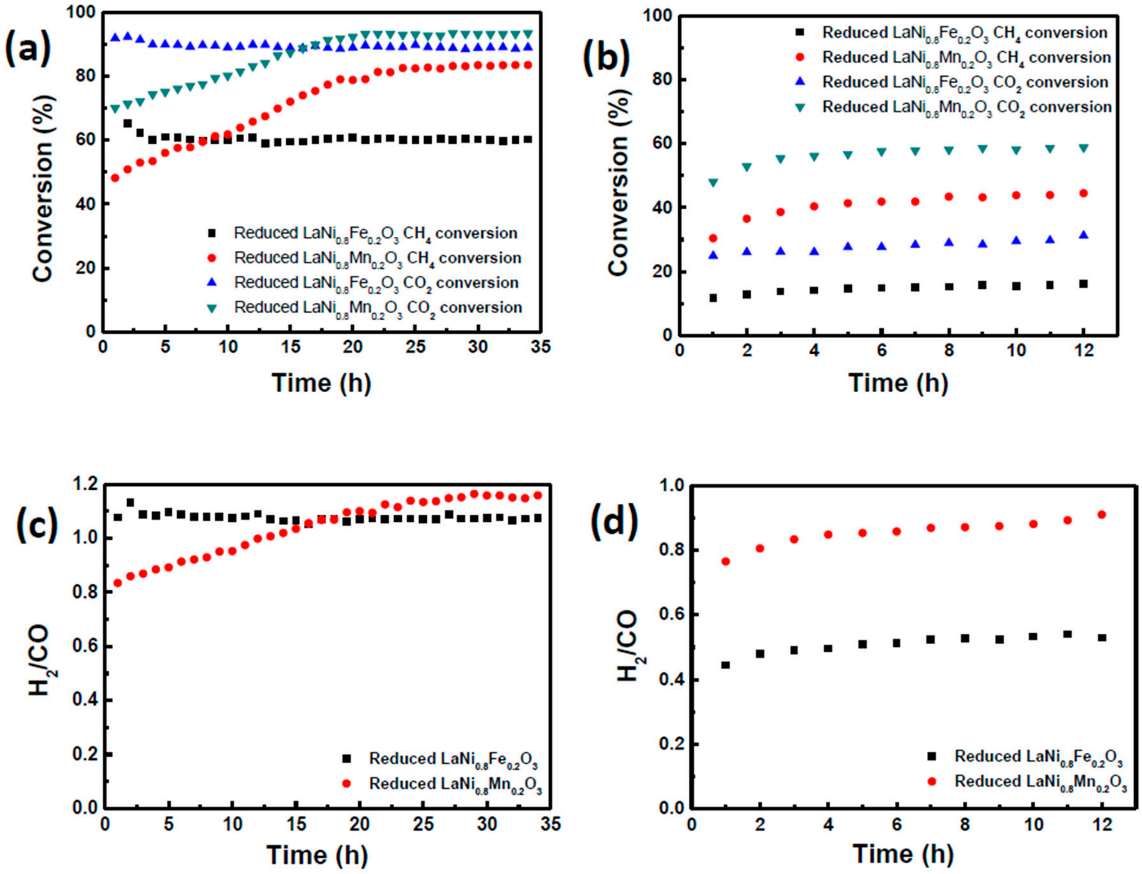

**Figure 4.** Conversion of methane and carbon dioxide of reduced $LaNi_{0.8}Fe_{0.2}O_3$ and $LaNi_{0.8}Mn_{0.2}O_3$ catalysts at (**a**) 800 °C and (**b**) 650 °C. $H_2$:CO product ratio of reduced $LaNi_{0.8}Fe_{0.2}O_3$ and $LaNi_{0.8}Mn_{0.2}O_3$ catalysts at (**c**) 800 °C (**d**) at 650 °C.

By contrast, the reduced $LaNi_{0.8}Mn_{0.2}O_3$ catalyst showed a slow increase in conversion up until 20 h of reaction and then stabilized at 80% $CH_4$ conversion. Both the catalysts showed that the $H_2$:CO product ratio is close to 1 at 800 °C (Figure 4c). The conversion rates for the $LaNi_{0.8}Mn_{0.2}O_3$ catalyst were comparatively lower at 650 °C, yet the $H_2$:CO product ratio is maintained close to 1, indicating the temperature decrease impacted only the conversion but not the selectivity. In case of reduced $LaNi_{0.8}Fe_{0.2}O_3$ catalyst; however, the $H_2$:CO product ratio was close to 0.5, which was a consequence of the RWGS reaction over DRM reaction at 650 °C. This is explained due to the fact that the presence of Fe in the Ni metal particles favored the RWGS reaction [43], whereas exsolution from $LaNi_{0.8}Mn_{0.2}O_3$ produced only pure Ni nanoparticles.

In order to compare the coking and agglomeration resistance of both catalysts, the spent materials were analyzed with X-ray diffraction (XRD), scanning electron microscopy (SEM), transmission electron microscopy (TEM), and thermogravimetric analysis (TGA). The XRD patterns of exsolved and post-reaction catalysts are shown in Figure 5. From Figure 5a, we can see that the Ni-Fe alloy particles exsolved from $LaNi_{0.8}Fe_{0.2}O_3$ completely de-alloyed to form pure Ni particles during the DRM at 650 °C. Oxides of Fe formed during de-alloying via oxidation by $CO_2$ and appear to react with $La_2O_3$ in the support to regenerate $LaFeO_3$ per a mechanism suggested by Jacob et al. [44]. Interestingly, only minimal de-alloying of Fe was observed when DRM took place at 800 °C. This is explained by the fact that de-alloying is favored as the environment is more oxidizing as shown in Figure S3. The reduced $LaNi_{0.8}Fe_{0.2}O_3$ catalyst was heated to 800 °C in inert atmosphere and then exposed to a mixed environment of $H_2/CO_2$ at different ratios. As the oxidizing nature of the environment was increased by raising the $CO_2$ gas concentration, the Ni-Fe alloy de-alloyed to a pure Ni phase. High levels of methane conversion, as observed at 800 °C, produced significant amounts of hydrogen, which means the catalyst is exposed to a highly reducing atmosphere, thereby favoring the alloyed state. Catalysts based on lanthanum ferrates and pure nickel particles should then exhibit high initial conversion, which will drive Ni-Fe alloying and a subsequent lowering of the conversion, consistent with the catalytic data shown in Figure 4a. Figure 5b presents a comparison between the pure Ni and Ni-Fe alloys formed during DRM, and confirms that the Ni-Fe alloy does not appear to change with time between 12 and 34 h. This supports the stable catalytic activity observed after the initial decrease.

XRD patterns of fresh and spent Mn-substituted catalyst are shown below in Figure 5c. Unlike in the Fe-substituted sample, Mn did not alloy with exsolved Ni nanoparticles despite the fact that the binary phase diagram shows that the two metals are soluble in the concentration range Ni-80–100%/Mn between room temperature and 800 °C [45]. The presence of unalloyed Ni along with manganese oxide phases, which act as a basic promoter, may have also helped achieve higher conversion [46,47]. From Figure 5c, an apparent difference in redox behavior of manganese oxide phases was observed under DRM conditions at 650 °C and 800 °C. The MnO phase that was present after reduction was oxidized to $Mn_3O_4$ at 650 °C but existed as MnO at 800 °C due to the highly reducing environment produced at high conversions.

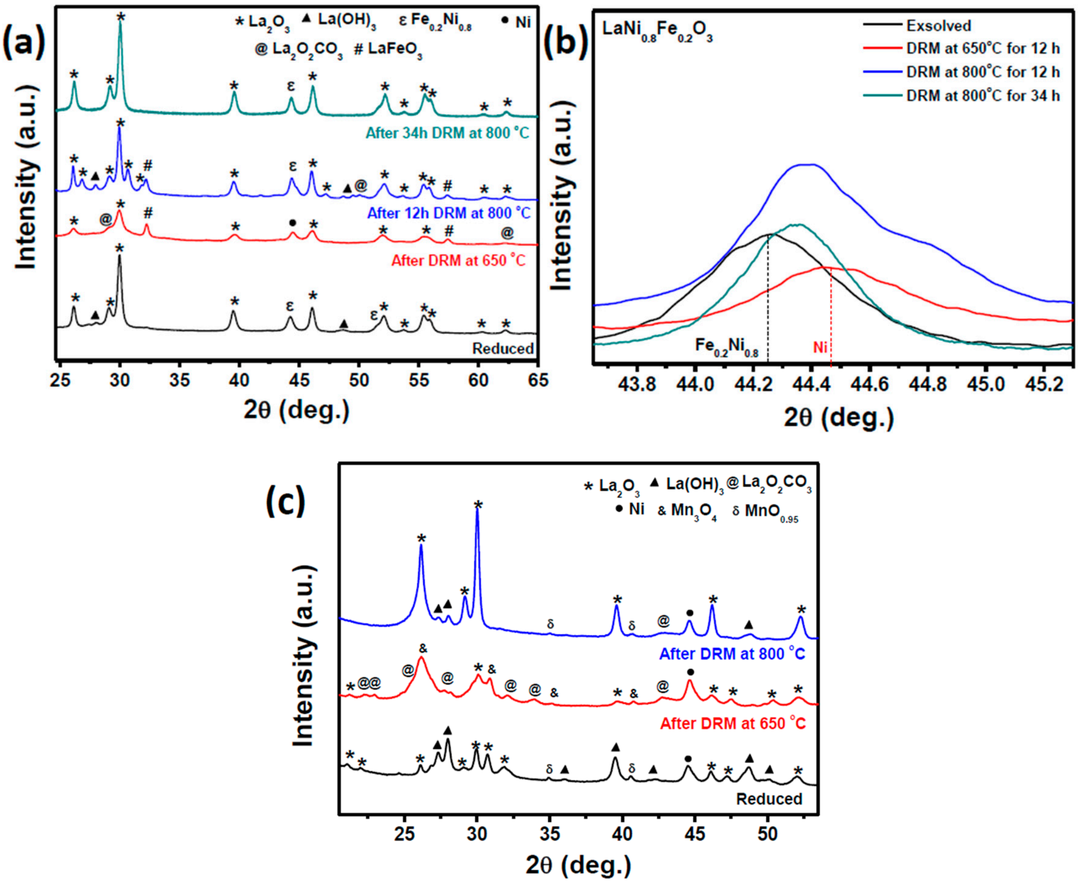

**Figure 5.** XRD patterns of reduced, after dry reforming reaction at 650 and 800 °C of (**a**) $LaNi_{0.8}Fe_{0.2}O_3$ and (**c**) $LaNi_{0.8}Mn_{0.2}O_3$ perovskites; formation of (**b**) Ni-Fe alloy at different reaction conditions of $LaNi_{0.8}Fe_{0.2}O_3$ perovskite.

An additional phase that was important to track during reaction was the formation of lanthanum oxycarbonate. This has been reported by us and others to prevent surface carbon by acting as an oxidizing agent [1,36]. Once the oxycarbonate phase is reduced (oxidizing the carbon), it can then be reformed by reaction with incoming $CO_2$ forming a redox loop ($La_2O_3 + CO_2 \rightleftarrows La_2O_2CO_3$).

We observed the quantity of oxycarbonate formation in both exsolved catalysts by thermogravimetric analysis (TGA) in a pure $CO_2$ environment. Prior to $CO_2$-TGA analysis, both the reduced catalysts were preheated to 800 °C in an inert atmosphere (to get rid of any hydrated species) and cooled to room temperature. From Figure 6a, it can be seen that the $La_2O_2CO_3$ formation starts at 550 °C for reduced $LaNi_{0.8}Mn_{0.2}O_3$ and at 570 °C for reduced $LaNi_{0.8}Fe_{0.2}O_3$. These temperatures are commensurate with oxycarbonate formation from $La_2O_3$ as previously reported [48]. From theoretical calculations, the full conversion $La_2O_3$ to $La_2O_2CO_3$ should yield 13.5% weight gain. However, the weight gain observed for reduced $LaNi_{0.8}Fe_{0.2}O_3$ catalyst is 8.2% and that for reduced $LaNi_{0.8}Mn_{0.2}O_3$ catalyst is 6%, indicating that, for both materials, not all of the $La_2O_3$ was converted to $La_2O_2CO_3$.

Similarly, the quantification of $La_2O_2CO_3$ phase during the DRM reaction was done by measuring the weight loss under an inert Ar atmosphere (Figure 6b) where the oxycarbonate decomposition was not masked by other oxidation reactions. The first weight loss observed at 300 °C is attributed to the decomposition of the lanthanum hydroxide $La(OH)_3$ phases observed in both post-reaction samples. The presence of this phase is due to residual moisture and the production of water via the RWGS reaction. The second prominent weight-loss observed between 600 °C and 750 °C is due to dissociation of $La_2O_2CO_3$ [48]. From Figure 6b, it is evident that there was more $La_2O_2CO_3$ present in reduced $LaNi_{0.8}Fe_{0.2}O_3$ samples compared to the reduced $LaNi_{0.8}Mn_{0.2}O_3$ DRM samples, consistent with the $CO_2$-TGA results (Figure 6a).

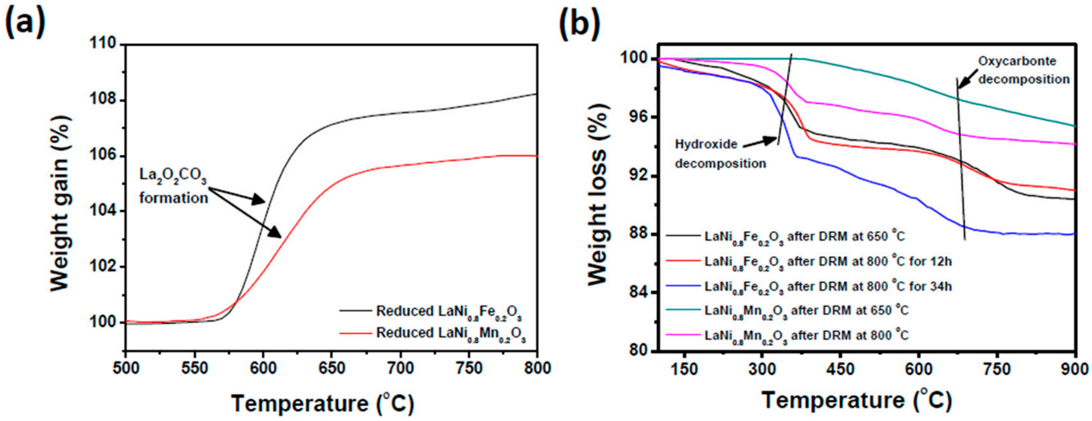

**Figure 6.** Thermogravimetric analysis of (**a**) reduced $LaNi_{0.8}Fe_{0.2}O_3$ and $LaNi_{0.8}Mn_{0.2}O_3$ catalysts in $CO_2$ atmosphere (**b**) $LaNi_{0.8}Fe_{0.2}O_3$ and $LaNi_{0.8}Mn_{0.2}O_3$ DRM samples in inert Ar atmosphere. All processes are labeled.

TEM imaging provided insight about the metal–support interaction, particle sintering, and coke formation after the DRM. The low-magnification TEM and SEM images of fresh (exsolved) and post-reaction catalysts are given in Figures S4 and S5. Both the micrographs suggest that there is no significant carbon accumulation in the catalyst exsolved from $LaNi_{0.8}Fe_{0.2}O_3$ for the DRM at 650 °C and 800 °C after 12 h, and only small amount of carbon after 34 h reaction at 800 °C. By contrast, catalysts derived by exsolution from $LaNi_{0.8}Mn_{0.2}O_3$ suffered severe coking after DRM reaction at both temperatures (Figure 7e and Figure S4).

Figure 7 shows electron micrographs of both catalysts before and after DRM reaction (at 800 °C). Figure 7a,d suggest that metal exsolved from $LaNi_{0.8}Fe_{0.2}O_3$ had a strong metal–support interaction, evidenced by the large interfacial area between the metal and support phases. In fact, this interaction may be so strong that the support partially covers the metal surface (Figure 7a), which leads to diminished activity through active-site blocking. Since carbon formation post-reaction was found here in the form of multi-walled carbon nanotubes (MWCNTs), this suggests that the tip-growth coking mechanism was occurring. Exsolution, which can increase the strength of the metal–support interaction compared to incipient wetness techniques, has been shown to block the progression of the tip-growth mechanism by strongly anchoring the Ni nanoparticle to the surface. Catalysts with weaker metal-support interactions are susceptible to the tip-growth mechanism since these particles can be lifted off the surface as shown in Figure 7e. Therefore, the difference in coke formation between the two samples may be related to the strength of the metal support interaction after exsolution. Furthermore, the particle size distribution analysis (Figure S6) shows that both the catalysts suffered from agglomeration.

The identity of phases in the support material labeled in Figure 7 came from XRD analysis shown in Figure 5, and is highlighted here to draw attention to the fact that the supporting oxide is in fact composed of many different phases. For both materials, the exsolution process produced lanthanum oxide ($La_2O_3$) as a result of releasing metal from the perovskite via reduction with hydrogen. Similarly, the presence of MnO and $Mn_3O_4$ was found by XRD in catalysts exsolved from $LaNi_{0.8}Mn_{0.2}O_3$.

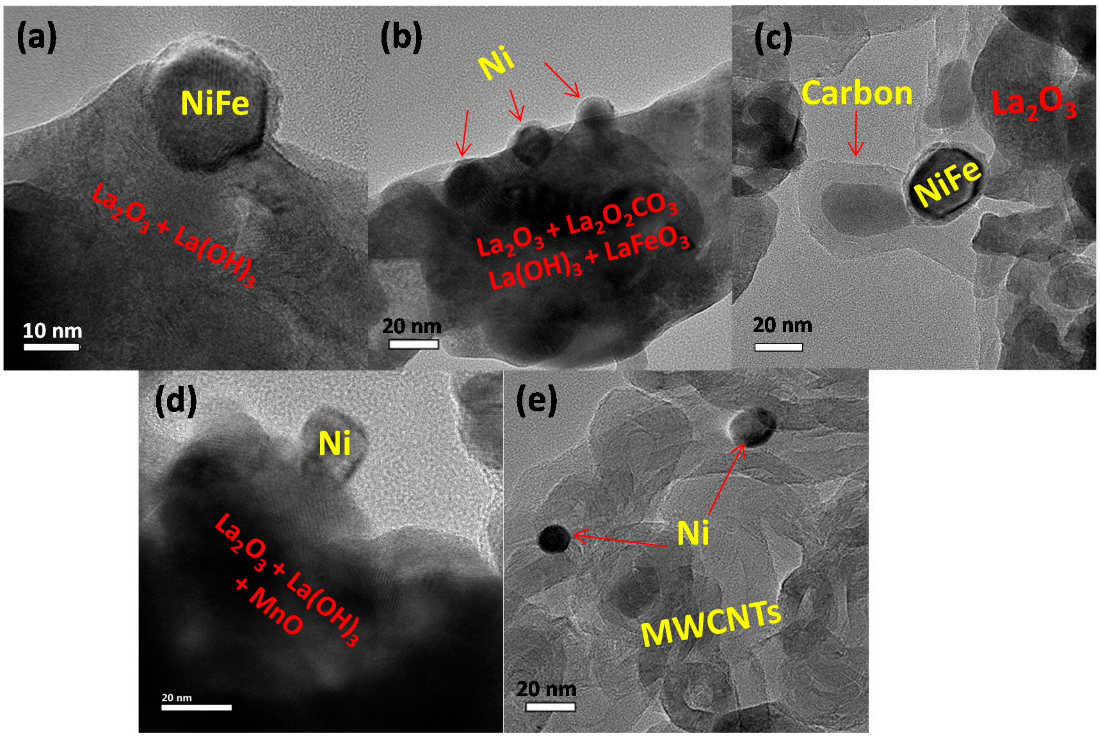

**Figure 7.** TEM images of the $LaNi_{0.8}Fe_{0.2}O_3$ perovskite (**a**) reduced, shows the exsolved Ni-Fe alloy from the perovskite; after dry reforming of methane (DRM) at 800 °C for (**b**) 12 h exsolved Ni particles are well socketed to the support after DRM and shows no carbon accumulation of spent catalyst, and (**c**) 34 h shows slight carbon accumulation of spent catalyst; high-resolution TEM images of $LaNi_{0.8}Mn_{0.2}O_3$ (**d**) reduced shows poor interaction of exsolved Ni crystal from the perovskite (new image added) (**e**) after DRM at 800 °C for 34 h shows the Ni particles surrounded by multi-wall carbon nanotubes (MWCNTs).

The quantity of coke formation during DRM on all catalysts was measured by TGA in an oxygen atmosphere and shown in Figure 8. A slight increase in weight observed at low temperatures in both reaction conditions is attributed to the oxidation of Ni. Weight loss of about 60% and 80% is observed in Mn-substituted catalyst after DRM reaction at 800 °C and 650 °C, respectively, corresponding carbon accumulated during DRM which is being oxidized to $CO_2$ in the TGA. Aside from the deep methane cracking mechanism which is endothermic, carbon formation is thermodynamically more favorable at lower temperatures and hence larger amounts of carbon were observed.

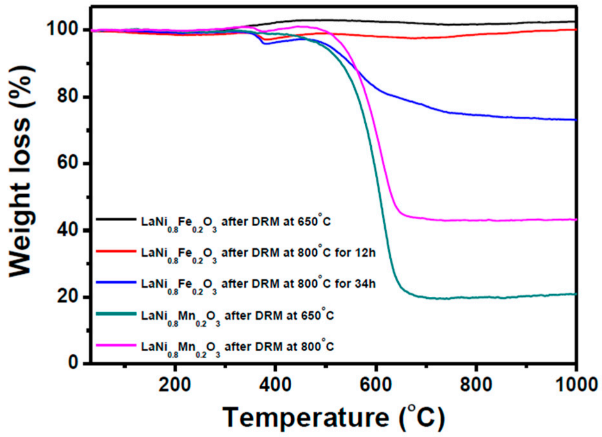

**Figure 8.** Thermo-gravimetric analyses of $LaNi_{0.8}Fe_{0.2}O_3$ and $LaNi_{0.8}Mn_{0.2}O_3$ spent catalysts in oxygen atmosphere.

TGA and TEM show that catalysts derived from the Fe-substituted perovskite, by contrast, had no carbon accumulation at 650 °C and 800 °C up to 12 h, and moderate accumulation after 34 h. XRD of this catalyst after 34 h revealed both the $LaFeO_3$ and $La_2O_2CO_3$ phases are not detectable (but were present after 12 h). This can be explained by a balance between two opposing effects; on the one hand, high methane conversion led to a more reducing atmosphere, but, in turn, this atmosphere diminished the presence of $LaFeO_3$ and $La_2O_2CO_3$, which both play a role in resisting carbon accumulation.

## 3. Materials and Methods

### 3.1. Synthesis

The Fe- and Mn-substituted $LaNiO_3$ catalysts were synthesized by the co-precipitation method reported previously with minor modifications [36]. All precursors were purchased through Alfa Aesar (Ward Hill, MA, USA) and had a purity of 99.9%. In a typical synthesis, appropriate ratios of metal nitrate salts using lanthanum nitrate hexahydrate ($La(NO_3)_3{\cdot}6H_2O$), nickel nitrate hexahydrate ($Ni(NO_3)_2{\cdot}6H_2O$), iron nitrate nonahydrate ($Fe(NO_3)_3{\cdot}9H_2O$, for Fe substitution), and manganese nitrate tetrahydrate ($Mn(NO_3)_2{\cdot}4H_2O$, for Mn substitution) were added in 100 mL of milli-Q water to obtain a 20 mM solution. Subsequently, the pH of the solution was maintained at pH 12 with drop-by-drop addition of 10 M aqueous sodium hydroxide (NaOH) under continuous stirring. The resultant slurry was refluxed at 75 °C for 6 h under vigorous stirring. The obtained precipitate was centrifuged and washed for 4–5 times with milli-Q water and ethanol, then dried overnight at 75 °C. $LaNi_{0.8}Fe_{0.2}O_3$ catalyst was obtained after calcination at 850 °C in air for 2 h and $LaNi_{0.8}Mn_{0.2}O_3$ catalyst was obtained after calcination at 750 °C in air for 2 h. The reported calcination temperature for each material was selected on the basis of which gave the highest purity material. The Brunauer-Emmett-Teller (BET) surface area of both perovskites was 18 $m^2/g$.

### 3.2. Materials Characterization

Powder X-ray diffraction (XRD) patterns were recorded by Bruker AXSD8 Advance (Billerica, MA, USA) with a Cu Kα radiation source. The microstructures of the catalysts were taken by e-SEM (Quanta 200 FEG ESEM) and TEM (Philips, Tecnai, operated at 200 kV). Temperature programmed reduction (TPR) experiment was performed on a Quantachrome, PulsarBET. Prior to the TPR measurement, the catalysts were degassed at 300 °C for 2 h. Thermo-gravimetric analysis (TGA) in oxygen was performed on a Netzsch STA 449 F5 Jupiter (Selb, Germany). The inert ($N_2$) and carbon dioxide TGA measurements were done on a Mettler Toledo SDTA851 (Lutz, FL, USA).

### *3.3. Testing of Catalysts Performance*

Prepared perovskites (50 mg) were plugged at the center of quartz tube (13 mm OD) with quartz wool. Before testing the catalytic activity, the perovskites were reduced at 800 °C for 2 h in 5 vol.% $H_2$/Ar. By this process, the active Ni phase was exsolved from the parent perovskite structure. The dry reforming performance of catalysts was tested at 650 and 800 °C by feeding a mixture of 1:1 molar ratio of $CH_4$ and $CO_2$ over the catalysts at a gas hourly space velocity (GHSV) of 13,700 mL/($g_{cat}$·h) without diluting gases. The conversion of methane and carbon dioxide into carbon monoxide and hydrogen was monitored using an SRI (USA) gas chromatograph fitted with packed 1/4" MS-13X and Hayesep-D columns. Hydrogen was detected using a nitrogen carrier and TCD detector. $CO_2$, CO, and $CH_4$ were detected by using helium carrier and TCD detector.

## 4. Conclusions

$LaNi_{0.8}Fe_{0.2}O_3$ and $LaNi_{0.8}Mn_{0.2}O_3$ catalysts were synthesized by a co-precipitation method and evaluated for dry reforming of methane at 650 °C and 800 °C. The physical properties of as synthesized and reduced perovskite phases do not show significant changes with the substitution of Fe or Mn at the B-site. Redox cycling showed that both catalysts were capable of exsolving active nanoparticles and were subsequently able to revive the original perovskite when exposed to an oxidizing atmosphere. Catalyst derived from $LaNi_{0.8}Mn_{0.2}O_3$ exhibited higher conversion rates in dry reforming of methane than those derived from $LaNi_{0.8}Fe_{0.2}O_3$. This is due to the fact that Mn metal did not co-exsolve with metallic Ni phase, but rather went towards the formation of MnO, which is a basic promoter for methane dry reforming. Despite the increased performance, catalysts derived from reduced $LaNi_{0.8}Mn_{0.2}O_3$ suffered from severe coke formation. The decrease in catalytic activity of Fe-substituted catalyst as compared to that of Mn-substituted catalyst was due to the presence of Fe-alloying with Ni; however, the Fe-substituted catalyst shows better coke resistance as compared to that of Mn-substituted catalyst due to the strong catalyst–support interactions. Although the $La_2O_2CO_3$ is a promoter for DRM reaction, we have not observed any significant affect in the present study.

**Supplementary Materials:** The following are available online at http://www.mdpi.com/2073-4344/10/1/27/s1, Figure S1: EDS mapping of as synthesized $LaNi_{0.8}Fe_{0.2}O_3$ perovskite, Figure S2: EDS mapping of as synthesized $LaNi_{0.8}Mn_{0.2}O_3$ perovskite, Figure S3: In-situ XRD of reduced $LaNi_{0.8}Fe_{0.2}O_3$ perovskite heated at 800°C in different ratios of $H_2$ and $CO_2$ atmospheres. The XRD shows that the de-alloying of Ni-Fe to pure Ni is more favorable in strong oxidizing atmosphere, Figure S4: TEM images of $LaNi_{0.8}Fe_{0.2}O_3$ perovskite (a) reduced, after DRM at 800 °C for (b) 12 h and (c) 34 h; TEM images of $LaNi_{0.8}Mn_{0.2}O_3$ perovskite (d) reduced and (e) after DRM at 800 °C for 34 h. Fe-substituted perovskite shows more resistant towards carbon accumulation than the Mn-substituted perovskite, Figure S5: SEM images of $LaNi_{0.8}Fe_{0.2}O_3$ perovskite after DRM at (a) 650 °C, (b) 800 °C, 12 h, and (c) 800 °C, 34 h; SEM images of $LaNi_{0.8}Mn_{0.2}O_3$ perovskite after DRM at (d) 650 °C and (e) 800 °C, Figure S6: Particle size distribution of both the catalysts before and after dry reforming reaction at 800 °C for 34 h: (a) $LaNi_{0.8}Fe_{0.2}O_3$ and (b) $LaNi_{0.8}Mn_{0.2}O_3$ catalysts. Average particle size with standard deviation is given in the graph.

**Author Contributions:** B.A.R. conceived and managed the project, reviewed all raw data, and drafted the manuscript with critical contributions from E.P.K. and I.K. E.P.K. and I.K. synthesized the materials and collected all of the materials characterization and catalytic data. All authors have read and agreed to the published version of the manuscript.

**Funding:** This work was funded by the Israeli Ministry of Energy grant 218-11-023, the Planning and Budgeting Committee/ISRAEL Council for Higher Education (CHE), and the Fuel Choice Initiative (Prime Minister Office of ISRAEL), within the framework of the "Israel National Research Center for Electrochemical Propulsion" (INREP). The APC was funded by INREP.

**Acknowledgments:** I.K. wants to thank Sarika Singh for her initial help in synthesis. All authors want to thank Tsion Ohaion Raz for helping to collect the TGA data in inert and $CO_2$ environments, Olga Shamis for helping in $O_2$-TGA measurements, and Gil Hayoun for assisting to build the catalytic experimental setup.

**Conflicts of Interest:** The authors declare no conflict of interest.

## References

1. Li, X.; Li, D.; Tian, H.; Zeng, L.; Zhao, Z.-J.; Gong, J. Dry reforming of methane over Ni/La2O3 nanorod catalysts with stabilized Ni nanoparticles. *Appl. Catal. B Environ.* **2017**, *202*, 683–694. [CrossRef]
2. Pakhare, D.; Spivey, J. A review of dry (CO2) reforming of methane over noble metal catalysts. *Chem. Soc. Rev.* **2014**, *43*, 7813–7837. [CrossRef]
3. Wang, S.; Lu, G.Q.; Millar, G.J. Carbon Dioxide Reforming of Methane to Produce Synthesis Gas over Metal-Supported Catalysts: State of the Art. *Energy Fuels* **1996**, *10*, 896–904. [CrossRef]
4. Cui, Y.; Zhang, H.; Xu, H.; Li, W. Kinetic study of the catalytic reforming of CH4 with CO2 to syngas over Ni/α-Al2O3 catalyst: The effect of temperature on the reforming mechanism. *Appl. Catal. A Gen.* **2007**, *318*, 79–88. [CrossRef]
5. Guczi, L.; Stefler, G.; Geszti, O.; Sajó, I.; Pászti, Z.; Tompos, A.; Schay, Z. Methane dry reforming with CO2: A study on surface carbon species. *Appl. Catal. A Gen.* **2010**, *375*, 236–246. [CrossRef]
6. Zubenko, D.; Singh, S.; Rosen, B.A. Exsolution of Re-alloy catalysts with enhanced stability for methane dry reforming. *Appl. Catal. B Environ.* **2017**, *209*, 711–719. [CrossRef]
7. Múnera, J.; Irusta, S.; Cornaglia, L.; Lombardo, E.; Vargascesar, D.; Schmal, M. Kinetics and reaction pathway of the CO2 reforming of methane on Rh supported on lanthanum-based solid. *J. Catal.* **2007**, *245*, 25–34. [CrossRef]
8. O'Connor, A.M.; Schuurman, Y.; Ross, J.R.; Mirodatos, C. Transient studies of carbon dioxide reforming of methane over Pt/ZrO2 and Pt/Al2O3. *Catal. Today* **2006**, *115*, 191–198. [CrossRef]
9. Liu, C.-J.; Ye, J.; Jiang, J.; Pan, Y. Progresses in the Preparation of Coke Resistant Ni-based Catalyst for Steam and CO2 Reforming of Methane. *ChemCatChem* **2011**, *3*, 529–541. [CrossRef]
10. Asencios, Y.J.; Assaf, E.M. Combination of dry reforming and partial oxidation of methane on NiO–MgO–ZrO2 catalyst: Effect of nickel content. *Fuel Process. Technol.* **2013**, *106*, 247–252. [CrossRef]
11. Ginsburg, J.M.; Piña, J.; El Solh, T.; De Lasa, H.I. Coke Formation over a Nickel Catalyst under Methane Dry Reforming Conditions: Thermodynamic and Kinetic Models. *Ind. Eng. Chem. Res.* **2005**, *44*, 4846–4854. [CrossRef]
12. Meille, V. Review on methods to deposit catalysts on structured surfaces. *Appl. Catal. A Gen.* **2006**, *315*, 1–17. [CrossRef]
13. Mitra, B.; Gao, X.; Wachs, I.E.; Hirt, A.M.; Deo, G. Characterization of supported rhenium oxide catalysts: Effect of loading, support and additives. *Phys. Chem. Chem. Phys.* **2001**, *3*, 1144–1152. [CrossRef]
14. Neagu, D.; Oh, T.-S.; Miller, D.N.; Ménard, H.; Bukhari, S.M.; Gamble, S.R.; Gorte, R.J.; Vohs, J.M.; Irvine, J.T. Nano-socketed nickel particles with enhanced coking resistance grown in situ by redox exsolution. *Nat. Commun.* **2015**, *6*, 8120. [CrossRef] [PubMed]
15. Wang, H.; Dong, X.; Zhao, T.; Yu, H.; Li, M. Dry reforming of methane over bimetallic Ni-Co catalyst prepared from La(CoxNi1-x)0.5Fe0.5O3 perovskite precursor: Catalytic activity and coking resistance. *Appl. Catal. B Environ.* **2019**, *245*, 302–313. [CrossRef]
16. Song, X.; Dong, X.; Yin, S.; Wang, M.; Li, M.; Wang, H. Effects of Fe partial substitution of La 2 NiO 4/LaNiO 3 catalyst precursors prepared by wet impregnation method for the dry reforming of methane. *Appl. Catal. A Gen.* **2016**, *526*, 132–138. [CrossRef]
17. Arandiyan, H.; Li, J.; Ma, L.; Hashemnejad, S.; Mirzaei, M.; Chen, J.; Chang, H.; Liu, C.; Wang, C.; Chen, L. Methane reforming to syngas over LaNixFe1−xO3 ($0 \leq x \leq 1$) mixed-oxide perovskites in the presence of CO2 and O2. *J. Ind. Eng. Chem.* **2012**, *18*, 2103–2114. [CrossRef]
18. Roseno, K.; Brackmann, R.; Da Silva, M.; Schmal, M. Investigation of LaCoO3, LaFeO3 and LaCo0.5Fe0.5O3 perovskites as catalyst precursors for syngas production by partial oxidation of methane. *Int. J. Hydrogen Energy* **2016**, *41*, 18178–18192. [CrossRef]
19. Gallego, G.S.; Batiot-Dupeyrat, C.; Barrault, J.; Florez, E.; Mondragón, F. Dry reforming of methane over LaNi1−yByO3±δ (B = Mg, Co) perovskites used as catalyst precursor. *Appl. Catal. A Gen.* **2008**, *334*, 251–258. [CrossRef]
20. Wei, T.; Jia, L.; Zheng, H.; Chi, B.; Pu, J.; Li, J. LaMnO3-based perovskite with in-situ exsolved Ni nanoparticles: A highly active, performance stable and coking resistant catalyst for CO2 dry reforming of CH4. *Appl. Catal. A Gen.* **2018**, *564*, 199–207. [CrossRef]

21. Yang, E.-H.; Noh, Y.S.; Hong, G.H.; Moon, D.J. Combined steam and CO2 reforming of methane over La1-xSrxNiO3 perovskite oxides. *Catal. Today* **2018**, *299*, 242–250. [CrossRef]
22. Rynkowski, J.; Samulkiewicz, P.; Ladavos, A.; Pomonis, P. Catalytic performance of reduced La2−xSrxNiO4 perovskite-like oxides for CO2 reforming of CH4. *Appl. Catal. A Gen.* **2004**, *263*, 1–9. [CrossRef]
23. Kim, W.Y.; Jang, J.S.; Ra, E.C.; Young Kim, K.; Kim, E.H.; Lee, J.S. Reduced Perovskite LaNiO3 Reduced perovskite LaNiO3 catalysts Modified with Co and Mn for Low Coke Formation in Dry Reforming of Methane. *Appl. Catal. A Gen.* **2019**, *575*, 198–203. [CrossRef]
24. Zhao, B.; Yan, B.; Yao, S.; Xie, Z.; Wu, Q.; Ran, R.; Weng, D.; Zhang, C.; Chen, J.G. LaFe0.9Ni0.1O3 perovskite catalyst with enhanced activity and coke-resistance for dry reforming of ethane. *J. Catal.* **2018**, *358*, 168–178. [CrossRef]
25. Steiger, P.; Nachtegaal, M.; Kröcher, O.; Ferri, D. Reversible Segregation of Ni in LaFe 0.8 Ni 0.2 O 3± δ During Coke Removal. *ChemCatChem* **2018**, *10*, 4456–4464. [CrossRef]
26. Steiger, P.; Delmelle, R.; Foppiano, D.; Holzer, L.; Heel, A.; Nachtegaal, M.; Kröcher, O.; Ferri, D. Structural Reversibility and Nickel Particle stability in Lanthanum Iron Nickel Perovskite-Type Catalysts. *ChemSusChem* **2018**, *10*, 2505–2517. [CrossRef]
27. Moradi, G.; Rahmanzadeh, M.; Khosravian, F. The effects of partial substitution of Ni by Zn in LaNiO3 perovskite catalyst for methane dry reforming. *J. CO2 Util.* **2014**, *6*, 7–11. [CrossRef]
28. Jahangiri, A.; Aghabozorg, H.; Pahlavanzadeh, H. Effects of Fe substitutions by Ni in La–Ni–O perovskite-type oxides in reforming of methane with CO2 and O2. *Int. J. Hydrogen Energy* **2013**, *38*, 10407–10416. [CrossRef]
29. Provendier, H.; Petit, C.; Kiennemann, A. Steam reforming of methane on LaNixFe1–xO3 (0≤x≤1) perovskites. Reactivity and characterisation after test. *Comptes Rendus l'Académie Sci. Ser. IIC Chem.* **2011**, *4*, 57–66. [CrossRef]
30. Yanagisawa, S.; Uozumi, A.; Hamada, I.; Morikawa, Y. Search for a Self-Regenerating Perovskite Catalyst Using ab Initio Thermodynamics Calculations. *J. Phys. Chem. C* **2013**, *117*, 1278–1286. [CrossRef]
31. Nishihata, Y.; Mizuki, J.; Akao, T.; Tanaka, H.; Uenishi, M.; Kimura, M.; Okamoto, T.; Hamada, N. Self-regeneration of a Pd-perovskite catalyst for automotive emissions control. *Nature* **2002**, *418*, 164–167. [CrossRef] [PubMed]
32. Hamada, I.; Uozumi, A.; Morikawa, Y.; Yanase, A.; Katayama-Yoshida, H. A Density Functional Theory Study of Self-Regenerating Catalysts LaFe1–xMxO3–y (M = Pd, Rh, Pt). *J. Am. Chem. Soc.* **2011**, *133*, 18506–18509. [CrossRef] [PubMed]
33. Singh, S.; Zubenko, D.; Rosen, B.A. Influence of LaNiO3 Shape on Its Solid-Phase Crystallization into Coke-Free Reforming Catalysts. *ACS Catal.* **2016**, *6*, 4199–4205. [CrossRef]
34. Shannon, R.T.; Prewitt, C.T. Effective ionic radii in oxides and fluorides. *Acta Crystallogr. Sect. B Struct. Crystallogr. Cryst. Chem.* **1969**, *25*, 925–946. [CrossRef]
35. Barsoum, M.; Barsoum, M. *Fundamentals of Ceramics*; CRC Press: Boca Raton, FL, USA, 2002.
36. Singh, S.; Prestat, E.; Huang, L.-F.; Rondinelli, J.M.; Haigh, S.J.; Rosen, B.A. Role of 2D and 3D defects on the reduction of LaNiO3 nanoparticles for catalysis. *Sci. Rep.* **2017**, *7*, 10080. [CrossRef]
37. Valderrama, G.; Kiennemann, A.; De Navarro, C.U.; Goldwasser, M.R. LaNi1-xMnxO3 perovskite-type oxides as catalysts precursors for dry reforming of methane. *Appl. Catal. A Gen.* **2018**, *565*, 26–33. [CrossRef]
38. Zhu, J.; Li, H.; Zhong, L.; Xiao, P.; Xu, X.; Yang, X.; Zhao, Z.; Li, J. Perovskite Oxides: Preparation, Characterizations, and Applications in Heterogeneous Catalysis. *ACS Catal.* **2014**, *4*, 2917–2940. [CrossRef]
39. Kontic, R.; Holzer, L.; Burnat, D.; Steiger, P.; Ferri, D.; Heel, A. Smart material concept: Reversible microstructural self-regeneration for catalytic applications. *J. Mater. Chem. A* **2016**, *4*, 11939–11948.
40. Nikoo, M.K.; Amin, N. Thermodynamic analysis of carbon dioxide reforming of methane in view of solid carbon formation. *Fuel Process. Technol.* **2011**, *92*, 678–691. [CrossRef]
41. Gallego, G.S.; Mondragón, F.; Barrault, J.; Tatibouët, J.-M.; Batiot-Dupeyrat, C. CO2 reforming of CH4 over La–Ni based perovskite precursors. *Appl. Catal. A Gen.* **2006**, *311*, 164–171. [CrossRef]
42. Batiot-Dupeyrat, C.; Valderrama, G.; Meneses, A.; Martinez, F.; Barrault, J.; Tatibouët, J.M. Pulse study of CO2 reforming of methane over LaNiO3. *Appl. Catal. A. Gen.* **2003**, *248*, 143–151. [CrossRef]
43. De Lima, S.M.; Assaf, J.M. Ni–Fe Catalysts Based on Perovskite-type Oxides for Dry Reforming of Methane to Syngas. *Catal. Lett.* **2006**, *108*, 63–70. [CrossRef]
44. Jacob, K.T.; Ranjani, R. Thermodynamic properties of LaFeO3−δ and LaFe12O19. *Mater. Sci. Eng. B* **2011**, *176*, 559–566. [CrossRef]

45. Ding, L.; Ladwig, P.F.; Yan, X.; Chang, Y.A. Thermodynamic stability and diffusivity of near-equiatomic Ni–Mn alloys. *Appl. Phys. Lett.* **2002**, *80*, 1186–1188. [CrossRef]
46. Chamoumi, M.; Abatzoglou, N.; Blanchard, J.; Iliuta, M.-C.; Larachi, F. Dry reforming of methane with a new catalyst derived from a negative value mining residue spinellized with nickel. *Catal. Today* **2017**, *291*, 86–98. [CrossRef]
47. Seok, S.-H.; Han, S.H.; Lee, J.S. The role of MnO in Ni/MnO-Al2O3 catalysts for carbon dioxide reforming of methane. *Appl. Catal. A Gen.* **2001**, *215*, 31–38. [CrossRef]
48. Bakiz, B.; Guinneton, F.; Arab, M.; Benlhachemi, A.; Villain, S.; Satre, P.; Gavarri, J.-R. Carbonatation and Decarbonatation Kinetics in the La2O3-La2O2CO3System under CO2Gas Flows. *Adv. Mater. Sci. Eng.* **2010**, *2010*, 1–6. [CrossRef]